

I provided a preliminary response to Heimsath and Whipple on Sept 25. Below is a brief summary of the main points of the Heimsath and Whipple review and my revised responses.

My P\_0 estimates are simply the residuals obtained from the regressions of Heimath et al. (2012). Far from being “inappropriate” and “unwise” (reviewer 1), “kooky” and “akin to data fabrication” (reviewer 2), or any of the other descriptions employed by the reviewers, computing residuals and testing for additional controls is a recommended step in regression analysis. Heimsath and Whipple define P\_0 as the y intercept of regression of soil production rates to soil thickness. This definition excludes the residuals of the regression without any basis. I define P\_0 (in the first sentence of the abstract and again in the first sentence of the introduction) as the maximum soil production rate at each point on Earth’s surface. My definition honors the fact that P\_0 values may vary continuously in space and that regressions of soil production rates to soil thickness yield a set of residuals that can and should be tested for additional controls. Residuals are estimates, since the regression used to compute the residuals has uncertainty. However, the fact that there is local variability in P values and uncertainty in 10Be measurements does not provide a basis for ignoring the residuals of this or any other regression. If local variability and/or data uncertainty dominate a soil production rate dataset, then no statistically significant landscape-scale controls will be identified in the residuals. For example, if large spatial variations existed in h\_0 (the decay length scale of the soil production function) in the SGM, P\_0 variations would be highly uncertain and controlling factors impossible to detect. However, Heimsath et al. (2012) estimated that h\_0 values differ by 0.05 m (0.32 m vs. 0.37 m) between portions of the SGM with the largest difference in P\_0 values. At a soil thickness of 30 cm, this difference corresponds to P\_0 differences of approximately 10% (i.e.,  $\exp(-0.30/0.32)$  vs.  $\exp(-0.30/0.37)$ ). This difference is more than 100 times smaller than the variation in P\_0 values. This difference becomes even smaller for soils thinner than 0.3 m.

Heimsath and Whipple question the processes included in my model. I have thought hard about what factors, besides variations in fault density and vegetation cover (and its associated wildfire regime), may explain the patterns in the data. Near-surface rocks in the SGM are in a highly compressive state (~10 MPa). In compressive-stress environments, the development of rugged topography leads to a reduction in compressive stress (and even the development of tensile stress in sufficiently steep areas) in the rocks beneath hillslopes. This change in stress state can increase the bulk porosity of the rock, allowing weathering agents to penetrate more readily into the rock, thus increasing the rate of weathering for a given soil thickness. In my proposed revision, I demonstrate that the predictions of the topographically induced stress fracture opening hypothesis are more consistent with the data than my previous model. This hypothesis has the benefit of a strong theoretical foundation. Once the data are modeled based on this hypothesis, temperature clearly emerges as a limiting factor for P\_0 values at the highest elevations of the range.

I regret not nailing this problem in the discussion paper and having to make major changes to the revision (in part because this entails more work for the reviewers). However, major changes were called for by the reviewers and a major overhaul of a manuscript is sometimes a positive outcome of negative reviews (the proposed revision to Section 2.1 is provided below and the proposed revision of the entire manuscript is provided as a separate document). I believe my revised paper provides a needed process-based understanding of the controls on P\_0 values documented by Heimsath et al. (2012) and establishes a climatic control on P\_0 values at the highest elevations of the SGM. These results provide a useful foundation for additional targeted 10Be analyses and for the incorporation of new methods that can further test the topographically induced stress fracture opening hypothesis (e.g., shallow seismic refraction surveys, 3D stress modeling, etc.).

In my opinion, the truth that has emerged from this review and my response is an interesting middle ground in which Heimsath et al. (2012) have been vindicated on their fundamental point that  $P_0$  values can increase with topographic ruggedness in some (i.e., compressive-stress) settings, but that also supports the hypothesis they rejected, i.e., that  $P_0$  values are controlled solely by climate and rock characteristics. The evidence remains that it is changes to rock characteristics, i.e., an increase in bedrock or intact regolith porosity in areas of more rugged topography, that lead to higher  $P_0$  values, together with a climatic limitation on  $P_0$  values at the highest elevations of the range.

Proposed revision to Section 2.1:

## 2.1 Controls on potential soil production rates in the SGM

$P_0$  values for the SGM can be estimated using the residuals obtained from the regression of soil production rates to soil thicknesses reported by Heimsath et al. (2012) (their Fig. 3). The exponential form of the soil production function quantifies the decrease in soil production rates with increasing soil thickness:

$$P = P_0 e^{-h/h_0}, \quad (1)$$

where  $h$  is soil thickness and  $h_0$  is a length scale quantifying the relative decrease in soil production rates for each unit increase in soil thickness. Heimsath et al. (2012) obtained  $h_0 = 0.32$  m for locations with an average slope,  $S_{av}$ , of less than or equal to  $30^\circ$  and  $h_0 = 0.37$  m for locations with  $S_{av} > 30^\circ$ .  $S_{av}$  is defined by Heimsath et al. (2012) as the average slope over hillslopes adjacent to each sample location.  $P_0$  values (Supplementary Table 1) can be estimated as the residuals obtained by dividing  $P$  values by the exponential term in equation (1):

$$P_{0,resid} = \begin{cases} Pe^{h/0.32 \text{ m}} & \text{if } S_{av} \leq 30^\circ \\ Pe^{h/0.37 \text{ m}} & \text{if } S_{av} > 30^\circ \end{cases} \quad (2)$$

where  $P_{0,resid}$  denotes  $P_0$  values estimated using the residuals of the regression. Note that equation (2) is equivalent to subtracting the logarithms of the exponential term from the logarithms of  $P$  values, since division is equivalent to subtraction under log transformation. Log transformation is appropriate in this case because  $P$  values are positive and positively skewed (i.e., there are many  $P$  values in the range of 50-200 m/Myr and a smaller number of values in the range of 200-600 m/Myr that would be heavily weighted in the analysis if the data were not log-transformed).  $P_{0,resid}$  values estimated from equation (2) increase, on average, with increasing  $S_{av}$  (Fig. 2A).  $P_{0,resid}$  values exhibit an abrupt increase at an  $S_{av}$  of approximately  $30^\circ$ .

Heimsath et al. (2012) did not include data points from locations without soil cover in their regressions because these data points appear (especially for areas with  $S_{av} > 30^\circ$ ) to fit below the trend of equation (1). This implies that a humped production function may be at work in some portions of the SGM. The mean value of  $P$  from areas with  $S_{av} \leq 30^\circ$  that lack soil cover is 183 m/Myr, i.e., slightly higher than, but within  $2\sigma$  uncertainty of, the  $170 \pm 10$

m/Myr value expected based on the exponential soil production function fit by Heimsath et al. (2012). As such, the evidence indicates that for areas with  $S_{av} \leq 30^\circ$ , data from locations with and without soil cover are both consistent with an exponential soil production function. The mean value of  $P$  from areas with  $S_{av} > 30^\circ$  that lack soil cover is 207 m/Myr, i.e., significantly lower than the  $370 \pm 40$  m/Myr expected based on the exponential soil production function. This suggests that a hump may exist in the soil production function for steep ( $S_{av} > 30^\circ$ ) slopes as they transition to a bare (no soil cover) condition. To account for this, I estimated  $P_0$  to be equal to  $1.78P$  (i.e., the ratio of 370 to 207) at locations with  $S_{av} > 30^\circ$  that lack soil cover.

The SGM has horizontal compressive stresses of  $\sim 10$  MPa in an approximately N-S direction at depths of less than a few hundred meters (e.g., Sbar et al., 1979; Zoback et al., 1980; Yang and Hauksson, 2013). The development of rugged topography can lead to topographically induced fracturing of bedrock and/or opening of pre-existing fractures in compressive-stress environments (e.g., Miller and Dunne, 1996; Martel, 2006; Slim et al., 2014; St. Clair et al., 2015). Given the pervasively fractured nature of bedrock in the SGM (e.g., Dibiase et al., 2015), I assume that changes in the stress state of bedrock or intact regolith beneath hillslopes leads to the opening of pre-existing fractures (i.e., an increase in the bulk porosity of bedrock or intact regolith) rather than the fracturing of intact rock. I adopt the analytic solutions of Savage and Swolfs (1986), who solved for the topographic modification of regional compressive stresses beneath ridges and valleys oriented perpendicular to the most compressive stress direction. Savage and Swolfs (1986) demonstrated that the horizontal stress ( $\sigma_{xx}$ ) in bedrock or intact regolith becomes less compressive under ridges as the slope increases (Fig. 3). In landscapes with a maximum slope larger than  $45^\circ$  (equivalent to an average slope of approximately  $27^\circ$  or  $\text{atan}(0.5)$  in the mathematical framework of Savage and Swolfs, 1986), bedrock or intact regolith that would otherwise be in compression develops tensile stresses close to the surface beneath hillslopes (Fig. 3A). An average slope of  $27^\circ$  is close to the threshold value of  $30^\circ$  that Heimsath et al. (2012) identified as representing the transition from low to high  $P_0$  values in the SGM. Therefore, the abrupt increase in  $P_{0,\text{resid}}$  values at approximately  $30^\circ$  is consistent with a transition from compression to tension in bedrock or intact regolith beneath hillslopes of the SGM. In addition to this sign change in the horizontal stress state in the rocks beneath hillslopes of the SGM, the Savage and Swolfs (1986) model predicts a gradual decline in horizontal compressive stress as  $S_{av}$  increases between 0 and approximately  $27^\circ$  (Fig. 3B):

$$\frac{\sigma_{xx}}{N_1} = \frac{2 - 4S_{av}}{(2 + 4S_{av})(1 + 4S_{av})} \quad (3)$$

where  $N_1$  is the regional maximum compressive stress and  $S_{av}$  has units of m/m in equation (3). Equation (3) is simply equation (36) of Savage and Swolfs (1986) expressed in terms of the average slope from the drainage divide to the location of maximum slope rather than the shape parameter  $b/a$  used by Savage and Swolfs (1986). Note that the tangent of the slope angle (units of m/m) is averaged to obtain  $S_{av}$  in all cases in this paper. However, after this averaging  $S_{av}$  is reported in degrees in some cases to facilitate comparison with the results of Heimsath et al. (2012).

Figure 3 illustrates the effects of topography on tectonic stresses only. Gravitational stresses can be included in the model by superposing the analytic solutions of Savage and Swolfs (1986) (their equations (34) and (35)) with the solutions of Savage et al. (1985) for the effects of topography on gravitational stresses (their equations (39) and (40)). The result is a three-dimensional phase space of solutions corresponding to different values of the regional tectonic stress  $N_1$ , the characteristic gravitational stress  $\rho g b$  (where  $\rho$  is the density of rock,  $g$  is the acceleration due to gravity, and  $b$  is the ridge height), and the Poisson ratio  $\mu$ . The effects of including gravitational stresses are (1) to increase the compression at depth via the lithostatic term (at soil depths this corresponds to an addition of  $\sim 10$  kPa, which is negligible compared to the regional compressive stress of  $\sim 10$  MPa in the SGM), and 2) to increase the compressive stresses near the point of inflection on hillslopes (e.g., Fig. 2a of Savage et al., 1985). These modifications do not alter the first-order behavior illustrated in Figure 3 for rocks close to the surface that are not close to hollows or other points of inflection. Section 3 provides additional discussion of the assumptions and alternative approaches to modeling topographically induced stresses.

The fit of the solid curve in Figure 2A to  $P_{0,resid}$  values is based on equation (3), together with an assumption that the transition from compressive to tensile stresses triggers an step increase in  $P_{0,resid}$  values over a small range of  $S_{av}$  values in the vicinity of the transition from compression to tension:

$$P_{0,S} = \begin{cases} P_{0,l} \left(1 - \frac{\sigma_{xx}}{N_1}\right) & \text{if } S_{av} \leq S_l \\ P_{0,h} \left(1 - \frac{\sigma_{xx}}{N_1}\right) & \text{if } S_{av} > S_h \\ \left(P_{0,l} + (P_{0,h} - P_{0,l}) \frac{S_{av} - S_l}{S_h - S_l}\right) \left(1 - \frac{\sigma_{xx}}{N_1}\right) & \text{if } S_l \leq S_{av} < S_h \end{cases} \quad (4)$$

where  $P_{0,S}$  denotes the model for the dependence of  $P_0$  values on  $S_{av}$ ,  $P_{0,l}$  and  $P_{0,h}$  are coefficients defining the low and high values of  $P_0$ , and  $S_l$  and  $S_h$  are the average slopes defining the range over which  $P_0$  values increase from low to high values across the transition from compression to tension.  $P_{0,l}$  and  $P_{0,h}$  were determined to be 170 m/Myr and 500 m/Myr based on least-squares minimization to the data (data from elevations above 2300 m were excluded because

of the climatic influence described below).  $S_l$  and  $S_h$  were chosen to be  $30^\circ$  and  $32^\circ$ , respectively, to characterize the abrupt increase in  $P_0$  values in the vicinity of  $30^\circ$ .

In addition to the average slope control associated with the topographically induced stress fracture opening process, a climatic control on  $P_0$  values can be identified using cluster analysis. This type of analysis involves identifying clusters in the data defined by distinctive values of the independent variables that also have different mean values of the dependent variable. The four points colored in blue in Figure 2A are the four highest elevation samples in the dataset, with elevations  $\geq 2300$  m a.s.l. The logarithms (base 10) of this cluster have a mean value of -0.40 after subtracting the logarithms of  $P_{0,S}$  to account for the average slope control on  $P_{0,resid}$  values, compared with a mean of 0.00 for the logarithms of the remaining data points with  $S_{av} > 30^\circ$  (also with the logarithms of  $P_{0,S}$  subtracted). Assuming a significance level of 0.05, the null hypothesis that the cluster of blue points has a mean that is indistinguishable from that of the remaining points with  $S_{av} > 30^\circ$  can be rejected based on the standard t test with unequal variances ( $t = 0.021$ ).

Figures 4A-4C illustrate the mean annual temperature (MAT), mean annual precipitation (MAP), and existing vegetation height (EVH) for the central portion of the SGM. Above elevations of approximately 1800 m a.s.l., vegetation height decreases systematically with increasing elevation (Fig. 4D). This limitation is likely to be primarily a result of temperature limitations on vegetation growth because MAP increases with elevation up to and including the highest elevations of the range. This result is consistent with the hypothesis that vegetation is a key driver of soil production. The decrease in  $P_0$  values with elevation is likely to be gradual rather than abrupt, and indeed there is evidence of a peak in the climatic control of  $P_0$  values. Figure 4E plots the ratio of  $P_{0,resid}$  to  $P_{0,S}$  as a function of elevation. The closed circles are binned averages of the data (each bin equals 100 m in elevation). The ratio of  $P_{0,resid}$  to  $P_{0,S}$  (equivalent to the residuals under log transformation after the effects of average slope are removed) increases, on average, and then decreases within the range of elevations between 1500 and 2600 m, broadly similar to the trend of EVH (Fig. 4D).

Local variability in  $P_0$  estimates due to variations in soil thickness, mineralogical variations within a given lithology, spatial variations in fracture density, etc. can be minimized by averaging  $P_0$  values (not including the four highest-elevation points because of the climatic control) from locations that have the same average slope (Fig. 2C). This process tends to average data from the same local cluster since local clusters often have average slopes that are both equal within the cluster and different from other clusters. Figure 2C demonstrates that the predictions of the

topographically induced stress fracture opening hypothesis are consistent with the observed dependence of  $P_{0,\text{resid}}$  values on  $S_{\text{av}}$  values.

The average slope and climatic controls on  $P_0$  values can be combined into a single predictive equation for  $P_0$  values:

$$P_{0,\text{pred}} = P_{0,s}C \quad (5)$$

where  $P_{0,\text{pred}}$  denotes predicted values for  $P_0$ ,  $C$  is a climatic index defined as 1 for  $z < 2300$  m and 0.4 (i.e., the ratio of the geometric mean of the data for  $z > 2300$  m to the remaining data points with  $S_{\text{av}} > 30^\circ$ ) for  $z > 2300$  m. A regression of  $P_{0,\text{pred}}$  values to  $P_{0,\text{resid}}$  values yields an  $R^2$  of 0.50 (Fig. 2D). When data with equal  $S_{\text{av}}$  values are averaged (i.e., the filled circles in Fig. 2D), the resulting  $R^2$  value is 0.87.

The results of this section demonstrate that average slope and climate exert controls on  $P_0$  values in the SGM. Although I did not find additional controls that were clearly distinct from these, it is worth discussing additional controls that I tested for. The data points colored in gray in Figure 2B are from the three rock types most resistant to weathering as determined by Spotila et al. (2002): granite, anorthosite, and the Mount Lowe intrusive suite. Spotila et al. (2002) also identified gabbro as a relatively resistant rock in the SGM, but no soil production rates are available from this rock type. Figure 2B suggests that lithology might exert some control on  $P_0$  values. Specifically, 7 samples from the more resistant lithologies sit above the least-squares fit of equation (4) to the data, while 13 (including the 7 lowest  $P_0$  values) sit below the least-squares fit. However, the null hypothesis that the residuals of the gray cluster after the effects of average slope are removed has a mean that is indistinguishable from the residuals of the remaining points (colored black in Figure 2B) cannot be rejected ( $t = 0.21$ ).

Many studies have proposed a relationship between fracture density and bedrock weatherability on the basis that fractures provide additional surface area for chemical weathering and pathways for physical weathering agents to penetrate into the bedrock or intact regolith (e.g., Molnar, 2004; Molnar et al., 2007; Goodfellow et al., 2014; Roy et al., 2016a,b). The difference in erosion rates between the SGM and adjacent San Bernardino Mountains, for example, has been attributed in part to differences in fracture density between these ranges (Lifton and Chase, 1992; Spotila et al., 2002). As such, it is reasonable to hypothesize that differences in  $P_0$  values might result from spatial variations in fracture density within each range. I computed a bedrock damage index  $D$  based on the concept that  $P_0$  values increase in bedrock that is more pervasively fractured, together with the fact that bedrock fracture densities are correlated with local fault density in the SGM (Chester et al., 2005; Savage and Brodsky, 2011). Savage and Brodsky (2011)

documented that bedrock fracture density decreases as a power-law function of distance from small isolated faults, i.e. as  $r^{-0.8}$  where  $r$  is the distance from the fault. Fracture densities around larger faults and faults surrounded by secondary fault networks can be modeled as a superposition of  $r^{-0.8}$  decays from all fault strands (Savage and Brodsky, 2011). Chester et al. (2005) documented similar power-law relationships between bedrock fracture density and local fault density in the SGM specifically. I define the bedrock damage index  $D$  (Fig. 5A) as the sum of the inverse distances, raised to an exponent 0.8, from the point where the  $D$  value is being computed to every pixel in the study area where a fault is located:

$$D = \sum_{\mathbf{x}'} \Delta x \left( \Delta x / |\mathbf{x} - \mathbf{x}'| \right)^{0.8} \quad (6)$$

where  $\Delta x$  is the pixel width,  $\mathbf{x}$  is the map location where bedrock damage is being computed, and  $\mathbf{x}'$  is the location of each mapped pixel in SGM where a fault exists.  $D$  has units of length since it is the sum of all fault lengths in the vicinity of a point, weighted by a power function of inverse distance. Equation (6) honors the roles of both the distance to and the local density of faults documented by Savage and Brodsky (2011) because longer faults and/or more mature fault zones with many secondary faults have more pixels that contribute to the summation. The fact that a relationship exists between  $P_{0,\text{resid}}$  values and  $D$  (Fig. 5B,  $p = 0.035$ ) and between  $D$  and  $S_{\text{av}}$  (Fig. 5C,  $p = 0.015$ ) suggests that some of the control by average slope that I have attributed to the topographically induced stress fracture opening process may reflect differences in the density of pre-existing fractures related to local fault density. However, the much higher  $R^2$  value of the relationship between  $P_{0,\text{resid}}$  and  $P_{0,\text{pred}}$  ( $R^2 = 0.50$ ) compared to that for the relationship between  $P_{0,\text{resid}}$  and  $D$  ( $R^2 = 0.08$ ) suggests that the topographically induced stress fracture opening process is the dominant mechanism controlling  $P_0$  values in the SGM. In addition, this process has a stronger theoretical foundation.

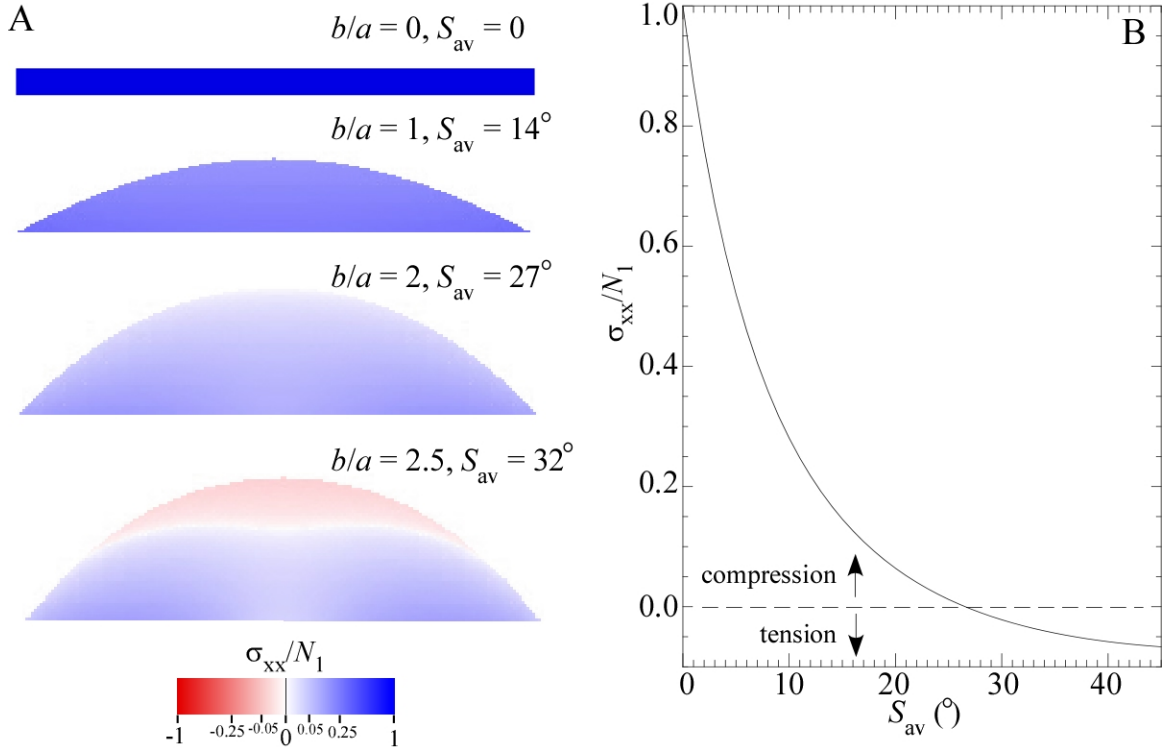


**Figure 2.** Analytic solutions illustrating the perturbation of a regional compressive stress field by topography. (A) Color maps of the horizontal normal stress,  $\sigma_{xx}$  (normalized to the regional stress,  $N_1$ ), as a function of ridge steepness (defined by the shape factor  $b/a$  of Savage and Swolfs (1986) and the average slope  $S_{av}$ ) using equations (34) and (35) of Savage and Swolfs (1986). The hillslopes are plotted with no vertical exaggeration. (B) Plot of  $\sigma_{xx}$  directly beneath the ridge as a function of  $S_{av}$  using equation (36) of Savage and Swolfs (1986). The plot illustrates the decrease in compressive stress with increasing average slope and the transition to tensile stresses at a  $S_{av}$  value of approximately  $27^\circ$ .

,

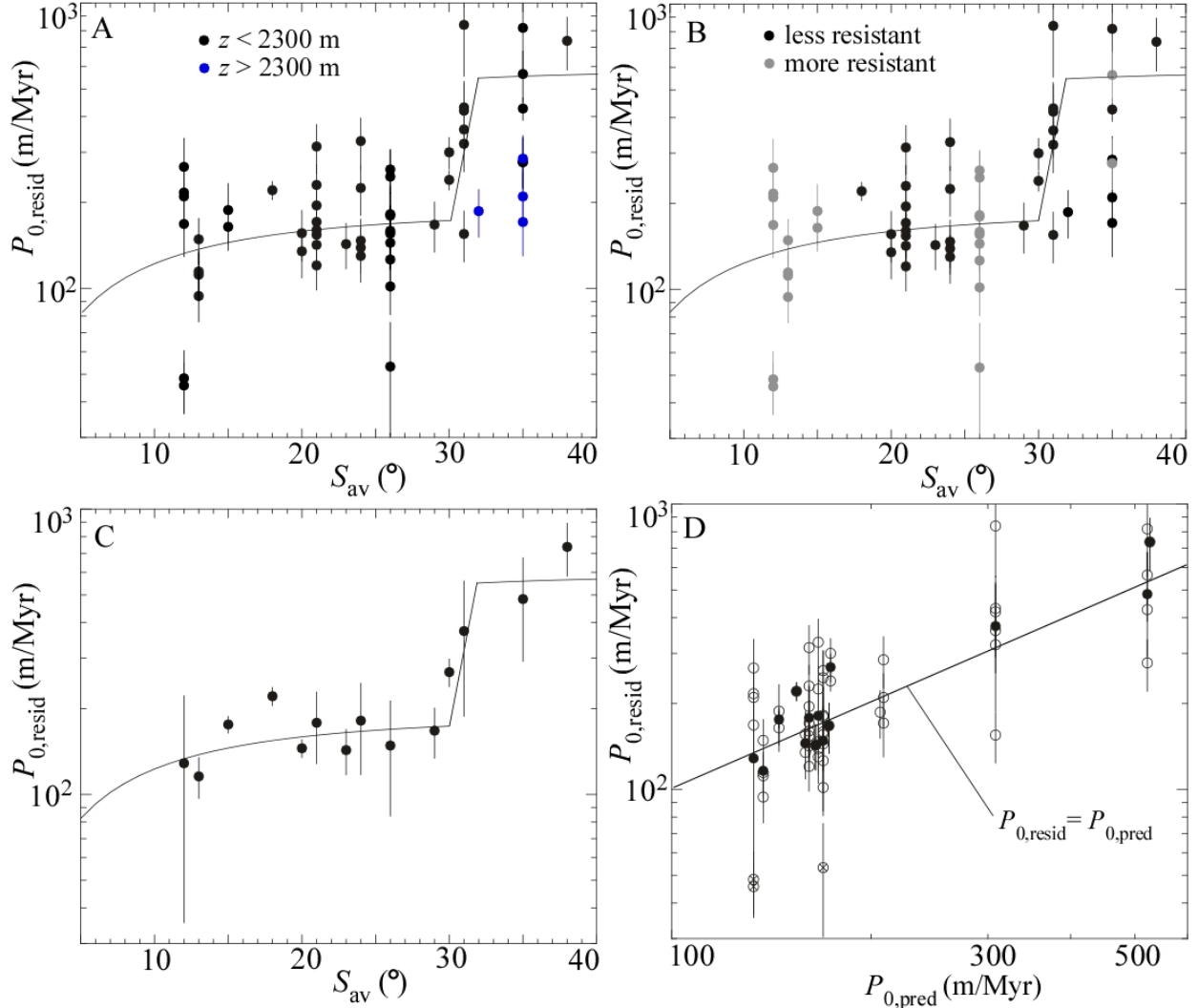


**Figure 3.** Plots of  $P_{0,\text{resid}}$  and their relationship to average slope,  $S_{\text{av}}$ , and other potential controlling factors. (A) Plot of  $P_{0,\text{resid}}$  values versus  $S_{\text{av}}$ . Data points colored blue are from the highest elevations of the range ( $z > 2300$  m). (B) The same plot as (A), except that data points are colored according to whether they from rocks that are relatively more resistant (gray) or less resistant (black) to weathering. (C) Plot of  $P_{0,\text{resid}}$  values averaged for each value of  $S_{\text{av}}$ . In (A) and (B), error bars represent the uncertainty of each data point, while in (C) the error bar represents the standard deviation of the data points averaged for each  $S_{\text{av}}$  value. (D) Plot of  $P_{0,\text{resid}}$  versus values predicted from equation (5). Unfilled circles show individual data points, while filled circles represent the averaged data plotted in (C).

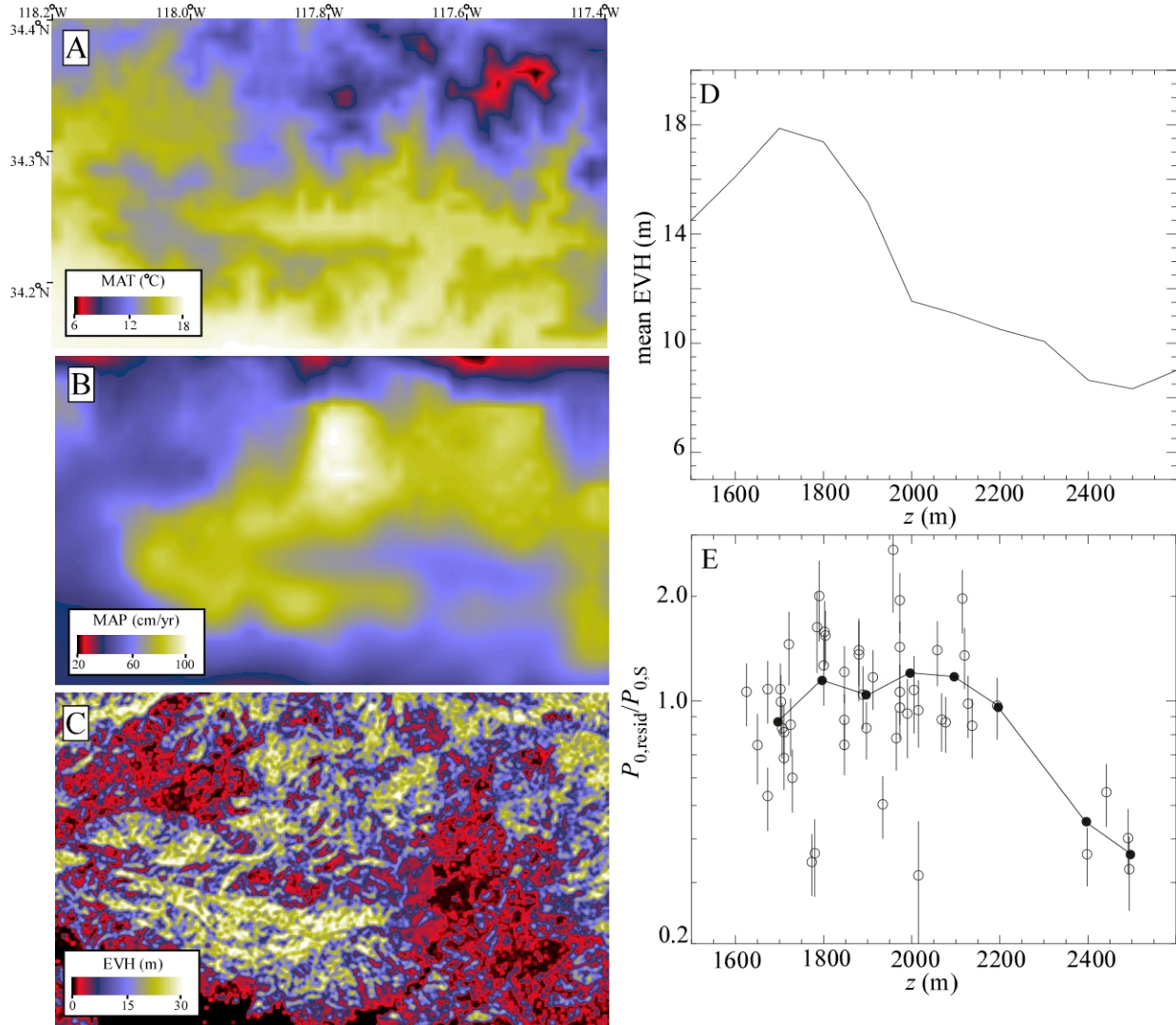


**Figure 4.** Climate and vegetation cover of the central San Gabriel Mountains. Color maps of (A) mean annual temperature (MAT) and (B) mean annual precipitation (MAP) from the PRISM dataset (Daly et al., 2001). (C) Color map of mean existing vegetation height (EVH) from the U.S. Geological Survey LANDFIRE database (U.S.G.S., 2016). (D) Plot of mean EVH versus elevation above sea level,  $z$ , using the data illustrated in (C). (E) Plot of the ratio of  $P_{0,\text{resid}}$  to  $P_{0,S}$  as a function of elevation. Filled circles are binned averages of the data (each bin equals 100 m in elevation).

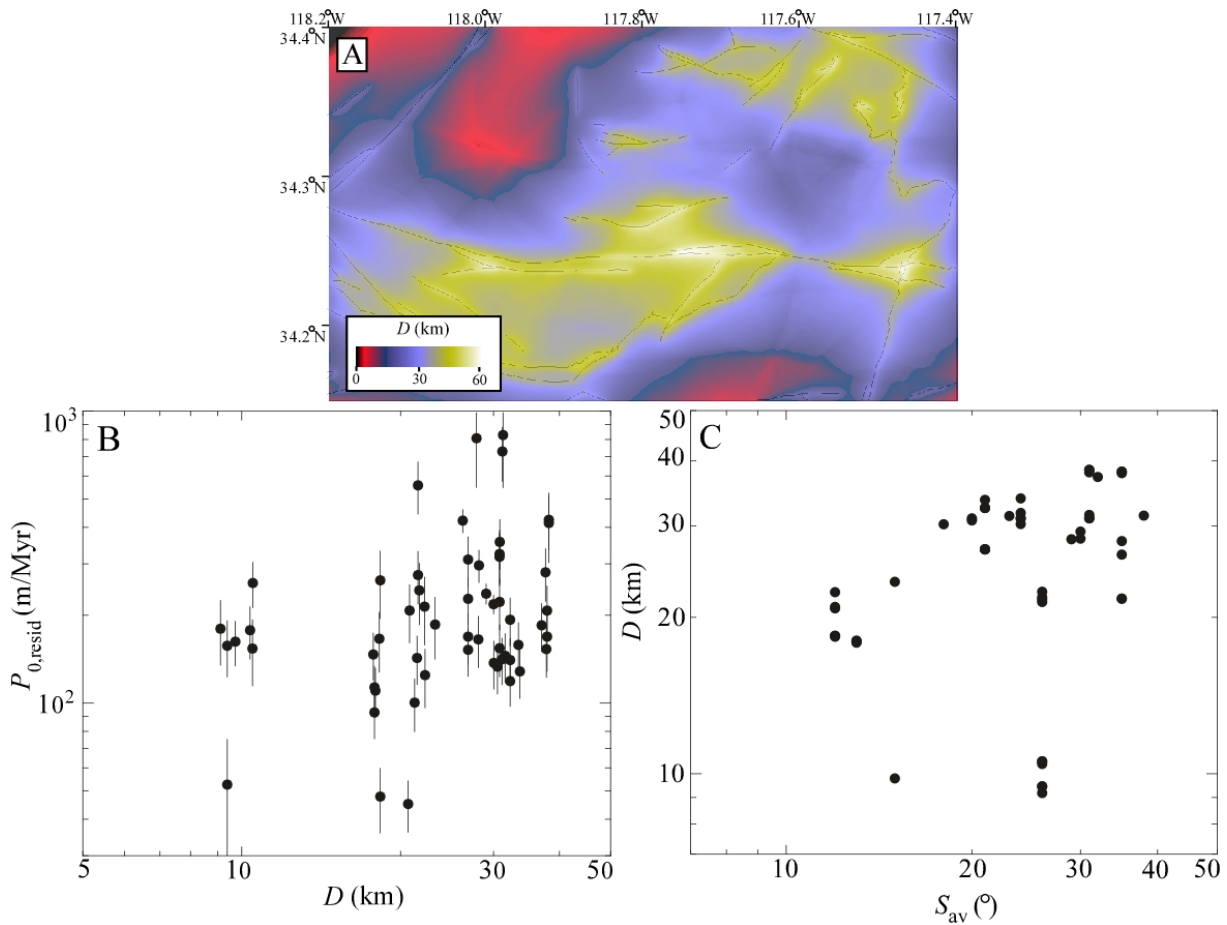


**Figure 5.** Map of the bedrock damage index,  $D$ , and its correlation with  $S_{\text{av}}$ . (A) Color map of spatial variations  $D$ . (B) Plot of  $D$  versus  $S_{\text{av}}$  for the 57 sample locations of Heimsath et al. (2012).